Proceedings of the Institution of Mechanical Engineers, Part J: Journal of Engineering Tribology
http://pij.sagepub.com/

Transient elastohydrodynamic point contact analysis using a new coupled differential deflection method Part 1: Theory and validation

M. J. A. Holmes, H. P. Evans, T. G. Hughes and R. W. Snidle

Proceedings of the Institution of Mechanical Engineers, Part J: Journal of Engineering Tribology 2003 217: 289
DOI: 10.1243/135065003768618641

The online version of this article can be found at:
http://pij.sagepub.com/content/217/4/289

Published by:
SAGE
http://www.sagepublications.com

On behalf of:
Institution of Mechanical Engineers
Institution of Mechanical Engineers

Additional services and information for *Proceedings of the Institution of Mechanical Engineers, Part J: Journal of Engineering Tribology* can be found at:

Email Alerts: http://pij.sagepub.com/cgi/alerts

Subscriptions: http://pij.sagepub.com/subscriptions

Reprints: http://www.sagepub.com/journalsReprints.nav

Permissions: http://www.sagepub.com/journalsPermissions.nav

Citations: http://pij.sagepub.com/content/217/4/289.refs.html

>> Version of Record - Apr 1, 2003

What is This?

Downloaded from pij.sagepub.com at Cardiff University on April 4, 2012

Transient elastohydrodynamic point contact analysis using a new coupled differential deflection method Part 1: theory and validation

M J A Holmes, H P Evans*, T G Hughes and **R W Snidle**
Mechanical Engineering and Energy Studies Division, Cardiff School of Engineering, Cardiff University, Cardiff, Wales, UK

Abstract: The paper presents a transient analysis technique for point contact elastohydrodynamic (EHL) lubrication problems using coupled elastic and hydrodynamic equations. Full coupling is made possible by use of a novel differential deflection formulation. The way in which the differential deflection is incorporated into the overall solution method for a point contact is discussed. A range of spatial and temporal discretization methods are incorporated and compared. The method is validated under transient conditions by a detailed comparison with published work produced using a different, independent method incorporating a moving roughness feature.

A comparison of the results with different discretization methods leads to the conclusion that spatial central differencing with a Crank–Nicolson temporal discretization is the most effective finite difference scheme, and this is generally equivalent to the finite element discretization given in detail in the paper. A comparison of the results produced for moving rough surfaces suggests that the finite element formulation is preferred.

Keywords: point contact EHL, non-Newtonian, transient, coupled method, differential deflection

NOTATION

A_b	height of the surface feature defined by equation (12) (m)
E'	effective modulus of elasticity (Pa)
$f_{i,j}$	pressure coefficient in the differential deflection equation (m^{-1})
F	factor determining timestep $= \bar{U}\Delta t/\Delta x$
h	film thickness (m)
h_0	constant in the film thickness equation (3) (m)
L	Moes and Bosma non-dimensional parameter $= \alpha E'[2\eta_0\bar{U}/(E'\bar{R})]^{1/4}$
M	Moes and Bosma non-dimensional parameter $= [w/(E'\bar{R}^2)][E'\bar{R}/(2\eta_0\bar{U})]^{3/4}$
n_c	number of neighbouring mesh points in discretization
N_i	shape function
p	pressure (Pa)
p_{hz}	maximum pressure in Hertzian contact (Pa)
P	$= p/p_{hz}$ in Figs 4 to 7
R_x, R_y	radii of relative curvature in axis directions (m)
$\bar{R}$	$2R_xR_y/(R_x + R_y)$ (m)
u	total deflection of the surfaces perpendicular to the xy plane (m)
$\bar{U}, \bar{V}$	mean surface velocities in axis directions (m/s)
w	load (N)
W_b	width of surface feature defined by equation (12) (m)
x, y	coordinates in the contact plane (m)
x_b	x coordinate of the centre of the ridge feature (m)
Z	parameter in the viscosity equation (5) $= \alpha/[\chi \ln(\eta_0/\kappa)]$
α	pressure viscosity coefficient (Pa^{-1})
γ	coefficient in the density equation (6) (Pa^{-1})
Δt	timestep (s)
$\Delta x, \Delta y$	mesh spacing in coordinate directions (m)
η	viscosity (Pa s)

The MS was received on 13 January 2003 and was accepted after revision for publication on 12 June 2003.
* *Corresponding author: Cardiff School of Engineering, Cardiff University, Queen's Buildings, The Parade, PO Box 925, Cardiff CF24 OYF, Wales, UK.*

Downloaded from pij.sagepub.com at Cardiff University on April 4, 2012

η_0	viscosity at ambient pressure (Pa s)
κ	coefficient in the viscosity equation (5) (Pa s)
λ	coefficient in the density equation (6) (Pa^{-1})
ξ	slide–roll ratio
ρ	density (kg/m^3)
ρ_0	density at ambient pressure (kg/m^3)
σ_x, σ_y	flow coefficients in axis directions (m s)
τ_0	non-Newtonian shear stress parameter (Pa)
ϕ	surface roughness feature (m)
χ	coefficient in the viscosity equation (5) (Pa^{-1})

1 INTRODUCTION

This paper presents a method for solving the elasto-hydrodynamic lubrication (EHL) point contact problem where the two equations describing the physics of the situation are solved as a coupled pair. The nature of the elastic deflection equation that is conventionally used in EHL analyses is such that the deflection at each point in a computational grid must be regarded as the weighted sum of the hydrodynamic pressures at *all* points in the grid.

Solving the hydrodynamic and elastic deflection equations simultaneously as a coupled pair is consequently impractical as the elastic equation is discretized into a 'full matrix' problem. The differential deflection approach presented by the authors [**1**, **2**] enables this full matrix difficulty to be eliminated. Application of the method in the less computationally demanding line contact configuration has proved to be highly effective [**3**] and has enabled results to be obtained for conditions taken from gear testing experiments [**4**] where the roughness features are an order of magnitude larger than the smooth surface film thickness that can be expected to develop between the components. Indeed, it has been possible to study features such as transient microcontact between asperity tips, and in-contact cavitation between successive asperity features has been found to occur in such analyses [**5**]. The current paper describes the extension of the coupled method to the point contact problem in which side-leakage effects occur and validation of the technique by comparison with published solutions [**6**] produced by an independent method.

Detailed EHL numerical solution schemes have been formulated for both line and point contact configurations over the last half century, with developments fuelled by the radical growth of computational power available to analysts. However, the 'full matrix' issue referred to above has generally meant that the numerical strategy adopted is one of sequential solution of the hydrodynamic equation and the elastic deflection equation. Relaxation techniques are used to systematically modify an initial approximation to the solution until a converged result is obtained that satisfies the two equations simultaneously. Since the elastic deflection within the contact is often an order of magnitude or more greater than the remaining film thickness it is clear that sequential solution of the two governing equations has been adopted on the basis of what is possible rather than what is desirable. The development of sequential solvers has been steady, starting with the pioneering work of Dowson and Higginson [**7**] for steady state line contacts and progressing to the sophisticated methods that are current for transient point contacts based on multilevel approaches [**6**], and incorporating fast Fourier transform calculation of the deflection [**8**], for example.

Very few workers have attempted to fully couple the elastic and hydrodynamic equations within an EHL solution scheme. Notable efforts in this area can be found [**9**, **10**], but further development has been generally seen as blocked by the intractable 'full matrix' problem. The key to the current development is the discovery [**1**] that the elastic equation can be specified in a differential form and that in this form the effect of pressure on the differential equation is spatially limited. This property can then be exploited to effectively fully couple the elastic and hydrodynamic equations. In the line contact implementation [**3**] this was achieved using a restricted bandwidth elimination solver. The bandwidth of the point contact problem depends on the number of mesh points in the computing area (in its smallest dimension). The point contact bandwidth thus remains large even though the influence of pressure on deflection is spatially very limited. Elimination methods have not, therefore, been adopted for the current work and a particular coupled iterative technique has been developed that solves the coupled equations very effectively. The solutions presented in the paper have been produced using this approach.

This paper is mainly concerned with the formulation, discretization and validation of the transient point contact coupled solution method incorporating the deflection equation in differential form. A companion paper presents results for rough surface conditions including ground surface features transverse to the entrainment direction, and confirms that the benefits of the method already observed in line contact solutions can also be obtained in the point contact case.

2 FUNDAMENTAL EQUATIONS

The hydrodynamic Reynolds equation is stated as

$$\frac{\partial}{\partial x}\left(\sigma_x \frac{\partial p}{\partial x}\right) + \frac{\partial}{\partial y}\left(\sigma_y \frac{\partial p}{\partial y}\right) - \frac{\partial(\rho \bar{U} h)}{\partial x} - \frac{\partial(\rho \bar{V} h)}{\partial y} - \frac{\partial(\rho h)}{\partial t} = 0 \quad (1)$$

Downloaded from pij.sagepub.com at Cardiff University on April 4, 2012

where σ_x and σ_y are given by $\sigma_x = \sigma_y = \rho h^3/(12\eta)$ for a Newtonian fluid model. For non-Newtonian situations, σ_x and $\sigma_y (\neq \sigma_x)$ are determined from the lubricant's pressure, pressure gradients, film thickness and surface velocities, as discussed in reference [**11**]. For the cases considered in the current paper, rolling and sliding take place in the x direction so that $\bar{U}$ is fixed and $\bar{V}$ is identically zero. Consequently, the cross-derivative pressure terms included in the Reynolds equation for general surface kinematics in reference [**11**] are not included and equation (1) may be written as

$$\frac{\partial}{\partial x}\left(\sigma_x \frac{\partial p}{\partial x}\right) + \frac{\partial}{\partial y}\left(\sigma_y \frac{\partial p}{\partial y}\right) - \bar{U}\left(\rho \frac{\partial h}{\partial x} + h\frac{\partial \rho}{\partial p}\frac{\partial p}{\partial x}\right) - \frac{\partial(\rho h)}{\partial t} = 0 \tag{2}$$

The film thickness is given by the expression

$$h(x, y) = \frac{x^2}{2R_x} + \frac{y^2}{2R_y} + u(x, y) + h_0 \tag{3}$$

The elastic deflection equation is utilized in the differential form developed by Evans and Hughes [**1**], so that over a regular discretization mesh

$$\frac{\partial^2 u(x_i, y_j)}{\partial x^2} + \frac{\partial^2 u(x_i, y_j)}{\partial y^2} = \frac{2}{\pi E'} \sum_{\text{all } k,l} f_{k-i,l-j} p_{k,l}$$

and the film thickness is related to the pressure distribution by the differential equation

$$\frac{\partial^2 h(x_i, y_j)}{\partial x^2} + \frac{\partial^2 h(x_i, y_j)}{\partial y^2} = \frac{1}{R_x} + \frac{1}{R_y} + \frac{2}{\pi E'} \sum_{\text{all } k,l} f_{k-i,l-j} p_{k,l} \tag{4}$$

A detailed derivation of the pressure influence factors $f_{i,j}$ for the differential deflection method is given in reference [**1**], where it is shown that the coefficients decay exceedingly rapidly as the indices increase from zero in comparison with the corresponding pressure influence coefficients for the conventional semi-infinite body deflection equation. In the differential form of the deflection equation, equation (4), the effect of pressure is thus extremely localized, which has enormous benefits in simultaneous numerical solution of equation (2) and (4).

Equations (2) and (4) are discretized as a coupled pair of differential equations to be solved simultaneously as described below. The non-linear dependence of viscosity and density on pressure are taken to be given by the well-known Roelands and Dowson and Higginson relationships respectively:

$$\eta = \eta_0 \exp\left\{\ln\left(\frac{\eta_0}{\kappa}\right)[(1 + \chi p)^z - 1]\right\} \tag{5}$$

$$\rho = \rho_0 \left(\frac{1 + \gamma p}{1 + \lambda p}\right) \tag{6}$$

These may be replaced by any other relationship that is appropriate for a given lubricant.

3 DISCRETIZATION

The equations are discretized on a rectangular mesh of points (x_i, y_j). Equation (4) is expressed using finite differences as

$$\frac{h_{i+1,j} + h_{i-1,j} - 2h_{i,j}}{\Delta x^2} + \frac{h_{i,j+1} + h_{i,j-1} - 2h_{i,j}}{\Delta y^2} = \frac{1}{R_x} + \frac{1}{R_y} + \frac{2}{\pi E'} \sum_{\text{all } k,l} f_{k-i,l-j} p_{k,l} \tag{7}$$

Equation (2) is discretized in a number of ways to allow for comparison between methods and with published reference material as discussed in later sections. The favoured form is obtained using linear finite elements (FEs) for the spatial discretization together with a standard Crank–Nicolson discretization of the time-dependent term. The Galerkin method to minimize the residual error over the finite element leads to equation (2) being expressed in the form

$$\int N_i \frac{\partial}{\partial x}\left(\sigma_x \frac{\partial p}{\partial x}\right) \mathrm{d}x\,\mathrm{d}y + \int N_i \frac{\partial}{\partial y}\left(\sigma_y \frac{\partial p}{\partial y}\right) \mathrm{d}x\,\mathrm{d}y - \bar{U} \int N_i \left(\rho \frac{\partial h}{\partial x} + h \frac{\partial \rho}{\partial p}\frac{\partial p}{\partial x}\right) \mathrm{d}x\,\mathrm{d}y - \int N_i \frac{\partial(\rho h)}{\partial t}\,\mathrm{d}x\,\mathrm{d}y = 0$$

where N_i are the four shape functions for the linear rectangular finite element adopted and the integrals are over the area of the element. The 'weak' formulation reduces the order of pressure gradient terms to give

$$\int \frac{\partial N_i}{\partial x}\left(\sigma_x \frac{\partial p}{\partial x}\right) \mathrm{d}x\,\mathrm{d}y + \int \frac{\partial N_i}{\partial y}\left(\sigma_y \frac{\partial p}{\partial y}\right) \mathrm{d}x\,\mathrm{d}y + \bar{U} \int N_i \left(\rho \frac{\partial h}{\partial x} + h \frac{\partial \rho}{\partial p}\frac{\partial p}{\partial x}\right) \mathrm{d}x\,\mathrm{d}y + \int N_i \frac{\partial(\rho h)}{\partial t}\,\mathrm{d}x\,\mathrm{d}y = 0$$

where the boundary integrals have been deleted since they cancel on internal element boundaries and are replaced with boundary conditions on the periphery of the solution. The pressure and film thickness terms are expressed as summations of their nodal values to give

$$\int \frac{\partial N_i}{\partial x}\left(\tilde{\sigma}_x \frac{\partial N_j}{\partial x} p_j\right) \mathrm{d}x\,\mathrm{d}y + \int \frac{\partial N_i}{\partial y}\left(\tilde{\sigma}_y \frac{\partial N_j}{\partial y} p_j\right) \mathrm{d}x\,\mathrm{d}y + \bar{U} \int N_i \left(\tilde{\rho} \frac{\partial N_j}{\partial x} h_j + \tilde{h} \frac{\partial \tilde{\rho}}{\partial p}\frac{\partial N_j}{\partial x} p_j\right) \mathrm{d}x\,\mathrm{d}y + \int N_i \frac{\partial}{\partial t}(\tilde{\rho} N_j h_j)\,\mathrm{d}x\,\mathrm{d}y = 0$$

Downloaded from pij.sagepub.com at Cardiff University on April 4, 2012

where the repeated suffix j indicates summation over the four nodal values and the symbol $\sim$ is used to indicate the average value obtained from the shape functions and current nodal values, which linearizes the problem. The Crank–Nicolson discretization of the time derivative between timesteps $m-1$ and m results in

$$\begin{aligned}
&\left[\frac{2}{\Delta t}\int N_i\tilde{\rho}N_j h_j \,\mathrm{d}x\,\mathrm{d}y + \int\frac{\partial N_i}{\partial x}\left(\tilde{\sigma}_x\frac{\partial N_j}{\partial x}p_j\right)\mathrm{d}x\,\mathrm{d}y\right.\\
&\quad+\int\frac{\partial N_i}{\partial y}\left(\tilde{\sigma}_y\frac{\partial N_j}{\partial y}p_j\right)\mathrm{d}x\,\mathrm{d}y\\
&\quad\left.+\bar{U}\int N_i\left(\tilde{\rho}\frac{\partial N_j}{\partial x}h_j+\tilde{h}\frac{\partial\tilde{\rho}}{\partial p}\frac{\partial N_j}{\partial x}p_j\right)\mathrm{d}x\,\mathrm{d}y\right]^m\\
&\quad=\left[\frac{2}{\Delta t}\int N_i\tilde{\rho}\tilde{h}\,\mathrm{d}x\,\mathrm{d}y-\int\frac{\partial N_i}{\partial x}\left(\tilde{\sigma}_x\frac{\partial\tilde{p}}{\partial x}\right)\mathrm{d}x\,\mathrm{d}y\right.\\
&\qquad-\int\frac{\partial N_i}{\partial y}\left(\tilde{\sigma}_y\frac{\partial\tilde{p}}{\partial y}\right)\mathrm{d}x\,\mathrm{d}y\\
&\qquad\left.-\bar{U}\int N_i\left(\tilde{\rho}\frac{\partial\tilde{h}}{\partial x}+\tilde{h}\frac{\partial\tilde{\rho}}{\partial p}\frac{\partial\tilde{p}}{\partial x}\right)\mathrm{d}x\,\mathrm{d}y\right]^{m-1}
\end{aligned}\tag{8}$$

These four equations ($i=1,2,3,4$) discretize the Reynolds equation to give an element fluid matrix with two degrees of freedom (h and p) at each node, and numerical Gauss point quadrature (2 by 2) is used to evaluate the area integrals. The global fluid matrix for the whole problem is then assembled using standard methods.

When assembled into an overall FE problem the equations for each node involve the pressure and film thickness values at the node and its eight surrounding neighbouring nodes. Thus the assembled equations (8) for the (i,j) node can be written in the form

$$\sum_{k=0}^{n_c}A_k p_k+\sum_{k=0}^{n_c}B_k h_k=R_{i,j}\tag{9}$$

where the suffix k represents the nodes contributing to the assembled equation at node (i,j) and $k=0$ denotes that node. A_k and B_k are the pressure and film variable coefficients for the Reynolds equation and n_c is the number of neighbouring nodes involved in the formulation.

The pressure summation in equation (7) is partitioned into those terms that involve the pressure at node (i,j) and its n_c neighbours, which are moved to the left-hand side, and the remainder, which are retained on the right-hand side. This equation can then be written in a corresponding form to equation (9) as

$$\sum_{k=0}^{n_c}C_k p_k+\sum_{k=0}^{n_c}D_k h_k=E_{i,j}\tag{10}$$

where C_k and D_k are the pressure and film variable coefficients for the differential deflection equation. [Clearly equation (7) requires that the D_k coefficients are zero for the neighbouring nodes which are diagonal to node (i,j).] The right-hand side, $E_{i,j}$, contains the pressure summation $\sum_{\text{all }k,l}f_{k-i,l-j}p_{k,l}$ for all pressure contributions except those incorporated in the first term on the left-hand side. The summation contributing to $E_{i,j}$ is split into two parts as $\sum_{\text{close}}f_{k-i,l-j}p_{k,l}+\sum_{\text{far}}f_{k-i,l-j}p_{k,l}$, so that at each point in the mesh there are three regions contributing to the pressure summation. The *near* region is that embodied on the left-hand side of equation (10), which corresponds to the point at which the equation is applied and its n_c nearest neighbours $(i\pm1,i\pm1)$. The *close* region is a square (or rectangular) area surrounding the near region and the *far* region makes up the remainder of the summation. The differential deflection formulation results in pressure weighting coefficients whose magnitudes fall rapidly to zero as their indices increase [**1**]. The contribution to $E_{i,j}$ from close and far contributions can be linearized as a result so that the coupled equations to be solved are equations (9) and (10). For the line contact formulation of this problem [**3**] an elimination solver was used to solve the equivalent pair of equations. For the point contact, however, equations (9) and (10) have a bandwidth equal to four times the number of mesh points in the narrowest grid dimension. This represents a formidable computational problem, and as is common in high mesh density FE problems, an iterative solution method is adopted. A simple Gauss–Seidel point iteration, where equation (9) is used as an iterative modification for pressure at node (i,j) and equation (10) as an iterative modification for film thickness, was found to be unstable and unsuitable. Instead, equations (9) and (10) are organized in the form

$$\begin{aligned}
A_0p_0+B_0h_0&=\hat{R}_{i,j}\left(=R_{i,j}-\sum_{k=1}^{n_c}A_kp_k-\sum_{k=1}^{n_c}B_kh_k\right)\\
C_0p_0+D_0h_0&=\hat{E}_{i,j}\left(=E_{i,j}-\sum_{k=1}^{n_c}C_kp_k-\sum_{k=1}^{n_c}D_kh_k\right)
\end{aligned}$$

which are regarded as a pair of iterative equations to be solved simultaneously for the updated values of p_0 and h_0 [i.e. the nodal values at node (i,j)]. The new iterative values at the node are thus

$$\begin{aligned}
p_{i,j}^{\text{new}}&=\frac{\hat{R}_{i,j}D_0-\hat{E}_{i,j}B_0}{A_0D_0-B_0C_0}\\
h_{i,j}^{\text{new}}&=\frac{\hat{E}_{i,j}A_0-\hat{R}_{i,j}C_0}{A_0D_0-B_0C_0}
\end{aligned}\tag{11}$$

and simple iteration using this pair of expressions is found to solve the coupled equations rapidly without any need of under-relaxation. The boundary of the near region can be extended by adopting a higher value of n_c, but this has been found to be unnecessary.

The boundary equations to be specified for the Reynolds equation are that pressure is everywhere

Downloaded from pij.sagepub.com at Cardiff University on April 4, 2012

positive and fixed at zero on the boundaries of the computing region. The boundary conditions required for equation (7) are values of h on the boundaries. These are obtained by applying equation (3) using the pressure distribution from the outer loop of the current timestep, with the deflection, u, on the boundary obtained from a discretized form of the conventional integral equation for deflection. Maintaining pressure at locations within the contact region where localized cavitation takes place within valley features does not strictly maintain continuity at these locations. Means of dealing with this situation in the iterative solver are under development using the simpler line contact situation and will be incorporated in the point contact method in due course. This factor is not thought to be significant as far as the results presented in this paper are concerned.

The coefficients C_k and D_k do not change during the solution. For the calculation of $h(x, y)$ and $p(x, y)$ at a particular timestep the following steps are involved:

1. Take the previous timestep as an initial approximation for p and h. Calculate the boundary values of h.
2. Evaluate $R_{i,j}$ from the values of p and h for the previous timestep.
3. Evaluate $E_{i,j}$ using the current approximation to p.
4. Evaluate the A_k and B_k coefficients for the Reynolds equation based on the current approximation to p and h.
5. Solve coupled equations (9) and (10) by iterative application of equations (11).
6. Re-evaluate the close contribution to $E_{i,j}$ and the boundary values for h based on the current approximation to p.
7. Repeat from step 4 until $p(x, y)$ and $h(x, y)$ are converged. Re-evaluate the far contribution to $E_{i,j}$ as necessary.

Comprehensive trials established that re-evaluation of the far contribution to $E_{i,j}$ is not necessary during the timestep. This would be the most time consuming aspect of the calculation for fine mesh problems were this not the case. The techniques of multilevel integration [**12**] or convolution integration via the Fourier transform [**13**] may both be used to accelerate the calculation of the far contribution to $E_{i,j}$, particularly as the kernel of the convolution integral is not singular. The calculations for the current paper were carried out on a 600 MHz workstation. For the most demanding problem considered of two rough surfaces with a grid of 800×100 mesh points and a spatial resolution of $a/200$ and $b/50$, the computing time is about 30 s per timestep. Half of this time is absorbed in the iterative solution of equations (9) and (10) and a quarter in the evaluation of the flow coefficients σ_x and σ_y. Both of these heavy computational demands could be substantially reduced but the authors have not pursued this avenue to date.

The differential deflection equation is specified as described above for all the cases considered in this work. Comparisons of different discretizations of the Reynolds equation are carried out within this same framework so that the solution scheme is general and the only differences between particular implementations are the number of coefficients used in equation (9) and their particular values. Four discretization schemes for the Reynolds equation were used: the FE formulation detailed above and three finite difference discretizations using central differences and two forms of backward difference for the first-order terms as advocated and used by Venner and Lubrecht [**6**] and others. Details of these formulations are specified in the Appendix.

4 RESULTS

The solution scheme was validated using a range of steady state point contact conditions and the transverse roughness feature modelled by Venner and Lubrecht [**6**] in both stationary roughness (steady state) and moving roughness (time-dependent) conditions. The extensive results presented by these authors for this case have been of great utility in enabling validation of the differential deflection technique against an entirely independent calculation method.

For steady state analyses five test cases were adopted that had operating conditions as given in Table 1. For steady state cases coefficient B_0 in the central difference representation of the Reynolds equation is zero. It is non-zero, but very small in comparison with other contributions, in the FE discretization. The backward difference schemes maintain a relatively high value for B_0 and as a result solutions are easier to obtain with these formulations. This situation is most apparent with steady state Newtonian high load conditions. When non-Newtonian conditions are introduced small amounts of sliding are sufficient to change the balance of terms in the formulations considerably, so that conclusions

Table 1 Specification of circular contact test cases

R_x (mm)	6.35
R_y (mm)	6.35
$\bar{U}$ (m/s)	0.21
E' (GPa)	227.3
η_0 (Pa s)	0.0096
α (GPa^{-1})	17.0
λ (GPa^{-1})	1.683
γ (GPa^{-1})	2.266
χ (GPa^{-1})	5.1
κ (Pa s)	63.15×10^{-6}

Case	w (N)	P_{hz} (GPa)	L	M
1	0.198	0.230	5	10
2	0.99	0.394	5	50
3	3.96	0.625	5	200
4	19.8	1.069	5	1000
5	99.0	1.829	5	5000

Downloaded from pij.sagepub.com at Cardiff University on April 4, 2012

reached as to optimum numerical formulations under Newtonian conditions no longer necessarily hold. The extent of the changes caused to the flow factors by introducing sliding in a Johnson and Tevaarwerk [**14**] non-Newtonian model with parameter $\tau_0 = 3\,\text{MPa}$ is illustrated in Fig. 1 for the example of test case 5. When ξ is zero both σ_x and σ_y have a value of 6.7×10^{-30} so that a 2 per cent level of sliding can be seen to increase the flow factors σ_x and σ_y by five orders of magnitude in the sliding direction (σ_x) and four orders of magnitude in the non-sliding direction (σ_y). Appropriate models for describing non-Newtonian behaviour remain a matter for debate, but this degree of reduction in effective viscosity causes significant differences to the numerical behaviour of the methods, and pure rolling/Newtonian conditions, for which many of the arguments in favour of backward difference formulations have been made, are really seen to be a very special case. Introducing time dependence removes the difficulties for all cases as B_0 is then of significant magnitude in comparison with other coefficients for appropriate timesteps [**15**].

For steady state Newtonian conditions backward difference formulations are found to be the most effective at high loads. For test case 5 these are the only formulations that produce smooth converged solutions with coarse meshes. This singular equation situation is not, however, of practical significance, as discussed above, although it has been the bane of numerical analysts studying Newtonian EHL problems for two generations or more. Figure 2 compares the central and minimum film thickness values for test case 4 obtained with all the discretization methods considered for a range of mesh discretisations, and shows that the

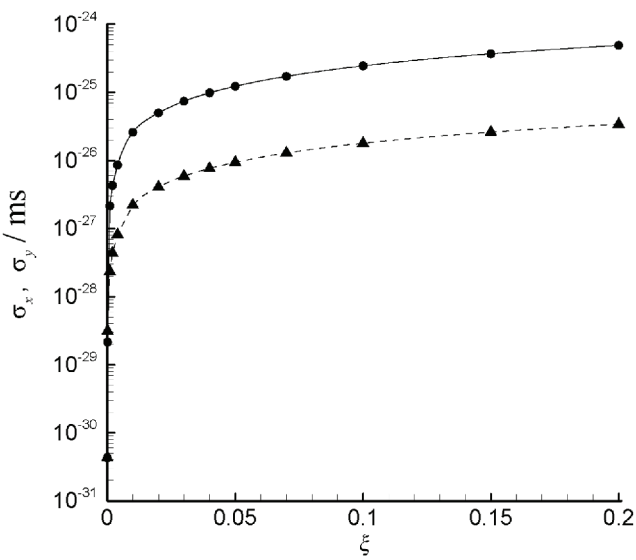

Fig. 1 Variation of flow factors σ_x (●) and σ_y (▲) for test case 4 with slide–roll ratio, ξ, for sliding in the entrainment direction x

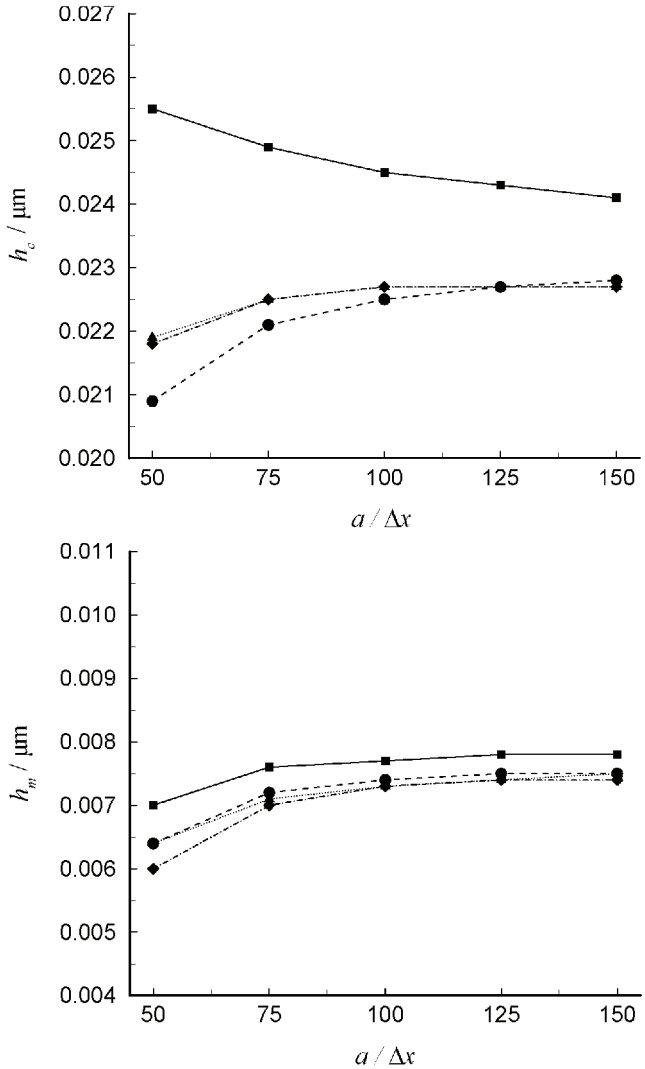

Fig. 2 Central h_c and minimum h_c film thickness values as a function of mesh refinement for test case 4; ▲ central difference, ◆ FE, ■ first-order backward, ● second-order backward. Note that ordinates have displaced zeros to aid comparison

second-order finite difference methods and the FE method behave in a very similar fashion. As pointed out by Venner and Lubrecht [**6**], the first-order backward difference method is less satisfactory and requires a very fine nodal structure to obtain the same answer as the other methods.

4.1 Validation under steady state conditions

The results for steady state, smooth cases with Newtonian conditions confirm the equivalence of the differential deflection formulation and the traditional method of treating deflection in point contact EHL solutions. The results correspond closely to published work using other methods (e.g. reference [**16**]). To

Downloaded from pij.sagepub.com at Cardiff University on April 4, 2012

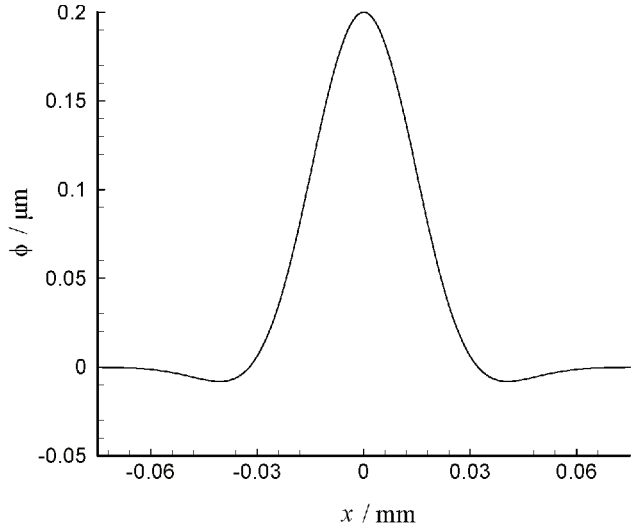

Fig. 3 Shape of ridge feature used for validation. (After Venner and Lubrecht [**6**])

validate the approach for rough surface conditions extensive comparison was made with the results published by Venner and Lubrecht [**6**] for the case of a transverse ridge added to one of the otherwise smooth contacting bodies. The ridge assumed is a modulated cosine wave that has the formula

$$\phi = A_{\mathrm{b}} \times 10^{-10[(x-x_{\mathrm{b}})/w_{\mathrm{b}}]^2} \cos\left(2\pi \frac{x - x_{\mathrm{b}}}{W_{\mathrm{b}}}\right) \tag{12}$$

The parameters chosen by Venner and Lubrecht [**6**] are $A_{\mathrm{b}} = 0.2\,\mu\mathrm{m}$ and $W_{\mathrm{b}} = 129\,\mu\mathrm{m}$, which produce a ridge height of $0.2\,\mu\mathrm{m}$ and an effective width of $70\,\mu\mathrm{m}$, as illustrated in Fig. 3.

For the validation exercise the Reynolds equation was discretized using the second-order backward difference method adopted by Venner and Lubrecht [**6**] with the same mesh resolution and computational mesh. The steady state result obtained using the current method without including the ridge was 5 per cent lower in central film thickness and 3 per cent lower in minimum film thickness than the corresponding quoted result. There was no significant difference in the pressure distributions obtained; each distribution supported the specified load and the calculated pressure values at the centre of the contact differed by less than 0.5 per cent. The small difference in film thickness probably results from the different elemental pressure forms used to discretize the deflection integral in the two methods. For the case analysed the deflection at the centre of the contact is 20 times the level of film thickness, so a 5 per cent difference in the calculated h_{c} value for notionally the same pressure distribution corresponds to a difference in the calculated deflection of the order of 0.25 per cent.

The EHL behaviour in simple sliding with the transverse ridge superimposed on the stationary surface was compared with the published data and shows all the features of those results [**15**]. Figure 4 compares the current results with the published ones at two particular ridge locations of $x_{\mathrm{b}} = \pm 0.5a$. The comparisons show that the results obtained are identical except for the same small difference in the magnitude of the film thickness.

4.2 Validation under transient conditions

For the transient case, a comparison was made with all of the conditions considered by Venner and Lubrecht [**6**]. Again the discretization of the Reynolds equation was identical to that used for the published results with a

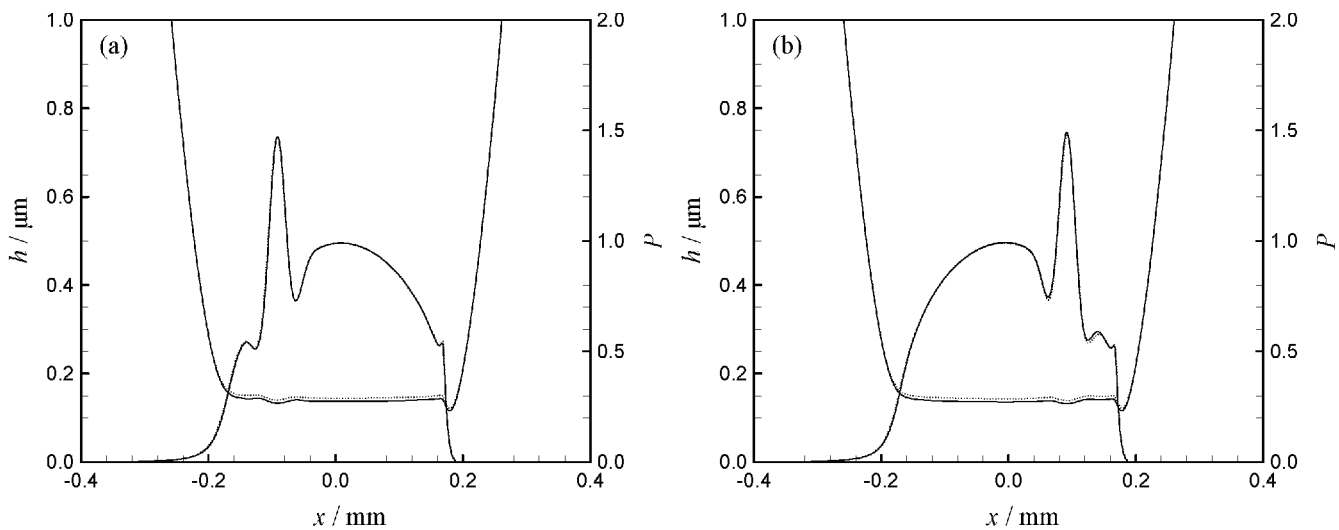

Fig. 4 Comparison of the stationary ridge case with published results: (a) $x_{\mathrm{b}} = -0.5a$, (b) $x_{\mathrm{b}} = 0.5a$. Dotted curves are from Venner (personal communication, 2002); solid curves are produced by the current method

Downloaded from pij.sagepub.com at Cardiff University on April 4, 2012

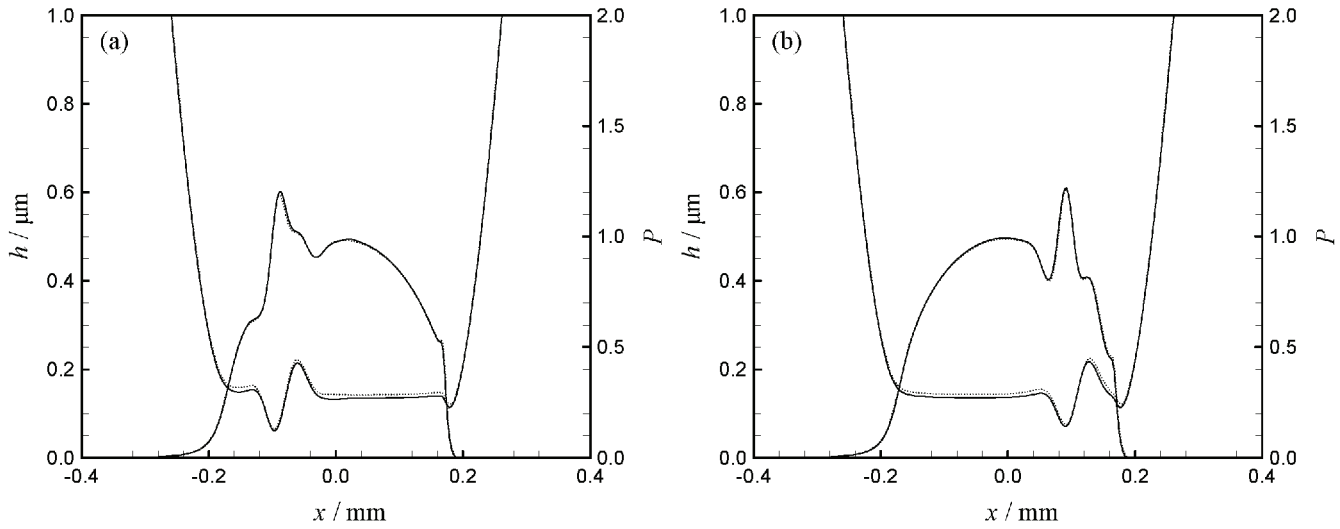

Fig. 5 Comparison of the transient pure rolling case with published results: (a) $x_b = -0.5a$, (b) $x_b = 0.5a$. Dotted curves are from Venner (personal communication, 2002); solid curves are produced by the current method

second-order backward difference scheme used for the squeeze-film term. Figure 5 compares the pressures and film thickness obtained when the ridge is again centred at $x_b = \pm 0.5a$ for the pure rolling case. The results obtained with the current method can again be seen to be almost identical to the reference case of Venner and Lubrecht [**6**], with the same very minor difference in film thickness. The pressure distribution and film thickness shapes can be seen to be identical. The comparisons described are regarded as sufficient to validate the accuracy of the current method. The authors are indebted to Dr C. H. Venner (personal communication, 2002) for providing more recent versions of the figures in reference [**6**] for the purposes of this comparison, which correct a minor contradiction between the method stated in reference [**6**] and the figures given in that paper.

The transient case was analysed using alternative formulations for the first-order spatial derivatives and the time derivative in comparative studies. The transient term in the Reynolds equation was discretized in two different ways, firstly using a second-order backwards difference formulation and secondly using the Crank–Nicolson method as described in section 3. The pure rolling transient example described above was recalculated using these alternative transient term representations and maintaining the second-order backward difference evaluation of the first-order spatial derivatives. A range of timestep values was adopted such that

$$\Delta t = \frac{F \Delta x}{\bar{U}}$$

with values of F taken as $F = 4$, 2, 1, 0.5, 0.25, 0.125, 0.0625 in turn for comparison. The finest timestep, where $F = 0.0625$, is used as a reference case. The differences between the methods at that resolution are

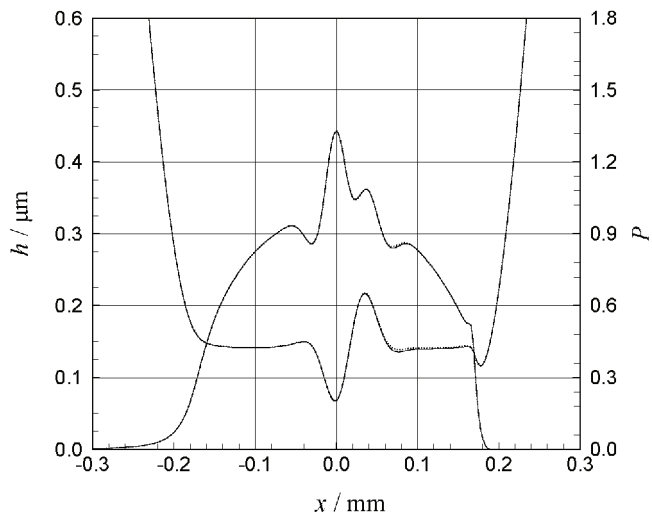

Fig. 6 Results at the ridge position $x_b = 0$ using the two time discretization methods with $F = 0.0625$; the dotted curve gives the second-order backward difference result; the solid curve gives the Crank–Nicolson result

seen to be very small, as shown in Fig. 6, which gives the results at the timestep where the ridge feature is centred at the origin, i.e. $x_b = 0$. The Crank–Nicolson result at this temporal resolution is used as the reference in comparing results for larger timestep values. Figure 7 shows the results obtained with the two discretization methods over the range of timestep values adopted. In all cases the timestep illustrated is that having $x_b = 0$, so that the profiles are directly comparable with the reference case. In general the Crank–Nicolson formulation approached the asymptotic solution with $F = 0.0625$ more rapidly as the timestep is reduced than does the backward difference formulation. Comparison of the results for $F = 2$, 1 and 0.5 suggests that the error

Downloaded from pij.sagepub.com at Cardiff University on April 4, 2012

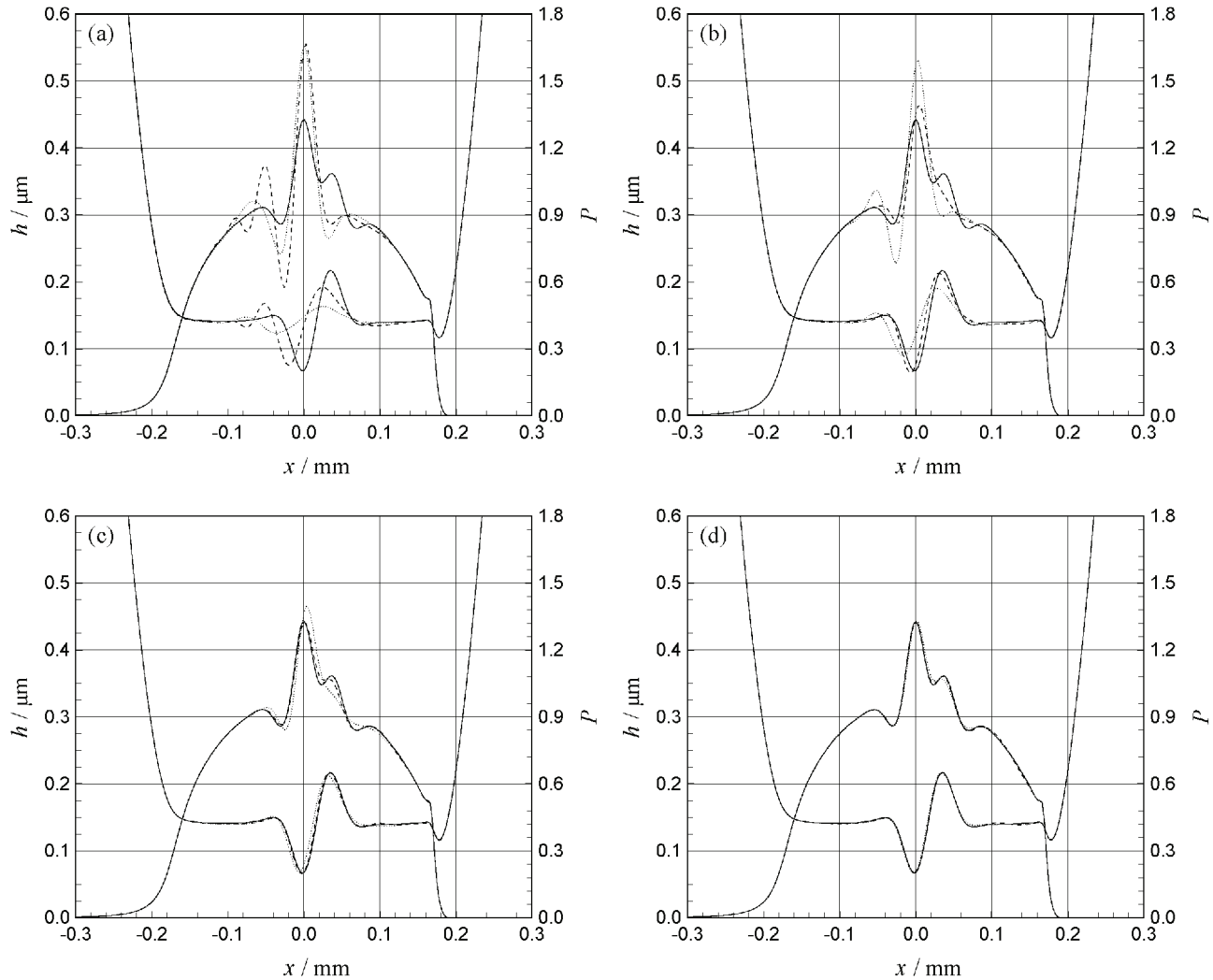

Fig. 7 Pressure and film thickness in pure rolling with $x_b = 0$ obtained with (---------) the Crank–Nicolson and (·····) the second-order backward difference temporal formulations at (a) $F = 4$, (b) $F = 2$, (c) $F = 1$, (d) $F = 0.5$. The reference solution for $F = 0.0625$ (———) is included for comparison

in the backward difference formulation corresponds to that in the Crank–Nicolson method when the timestep is twice as large. This observation might well be expected as the finite backward difference formulation is second-order accurate in Δt. The Crank–Nicolson approach, on the other hand, applies a central difference midway between timesteps, so that the temporal resolution may be expected to be second-order accurate in $\Delta t/2$. The error term in the second-order backward difference and Crank–Nicolson approximations are seen to be $(\Delta t^3/3)(\partial^3/\partial t^3)$ and $(\Delta t^3/24)(\partial^3/\partial t^3)$ respectively, so that the comparative behaviour of the two methods in Fig. 7 is consistent with the larger error involved in the second-order backward derivative at any given timestep. The practical conclusion is that the Crank–Nicolson scheme allows timesteps that are twice as large to be used without sacrificing accuracy. This temporal resolution method has therefore been adopted for the remainder of this study.

Comparisons were also carried out between second-order backward difference and central difference methods for approximating the first-order spatial derivatives in the Reynolds equation. The case considered was more heavily loaded than in the previous comparison with the conditions as specified in Table 1, but with $\bar{U} = 3.36\,\mathrm{m/s}$ and $w = 158.4\,\mathrm{N}$ so that the non-dimensional groups have values of $L = 10$ and $M = 1000$, and the maximum Hertzian pressure is 2.15 GPa. The contact had $\xi = 0.25$ and $\tau_0 = 3\,\mathrm{MPa}$ and a transverse ridge of the form of equation (12) with $A_b = 0.2\,\mu\mathrm{m}$ and $W_b = 0.75a$ on the faster moving surface.

The results obtained for the two methods with a spatial resolution of $\Delta_x = \Delta_y = a/150$ were indistinguishable and are shown as a reference in Figs 8 and 9 as solid lines. The timestep presented has the ridge centred at $x_b = 0.5a$. Figure 8 shows the way that the central difference method results approach the reference result for a sequence of mesh resolutions. The corresponding

Downloaded from pij.sagepub.com at Cardiff University on April 4, 2012

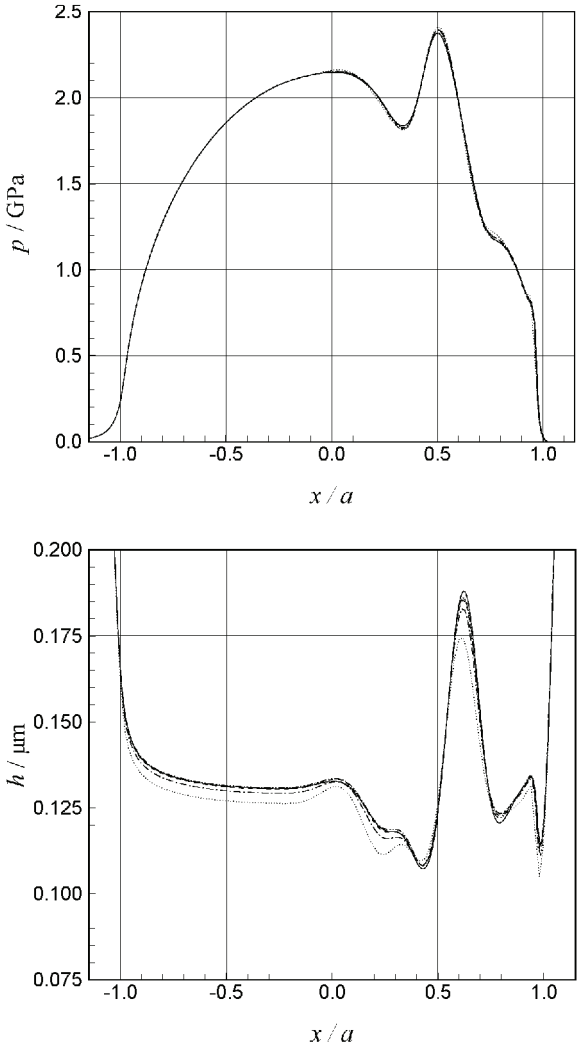

Fig. 8 Pressure (upper figure) and film thickness (lower figure) obtained using central differences for first-order derivatives at five mesh resolutions for the pure rolling case with $x_b = 0.5a$ for a Crank–Nicolson time discretization with $F = 1.0$. Cases shown are (·····) $a/\Delta x = 50$, (–·–·–) $a/\Delta x = 75$, (---------) $a/\Delta x = 100$, (–··–··–) $a/\Delta x = 125$, (———) $a/\Delta x = 150$

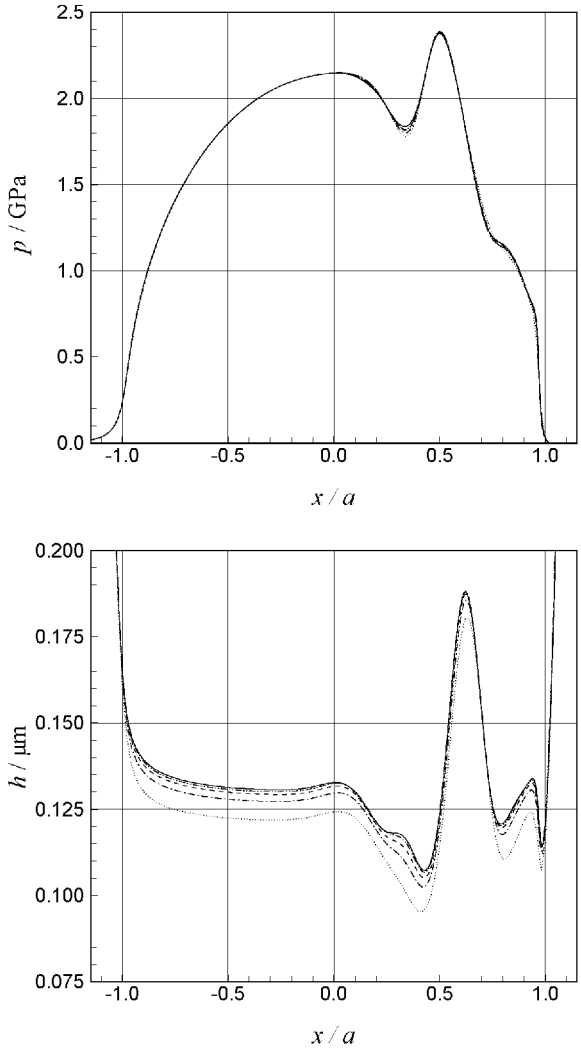

Fig. 9 Pressure (upper figure) and film thickness (lower figure) obtained using second-order backward differences for first-order derivatives at five mesh resolutions for the pure rolling case with $x_b = 0.5a$ for the Crank–Nicolson time discretisation with $F = 1.0$. Cases shown are (·····) $a/\Delta x = 50$, (–·–·–) $a/\Delta x = 75$, (---------) $a/\Delta x = 100$, (–··–··–) $a/\Delta x = 125$, (———) $a/\Delta x = 150$

results for the second-order backward method are shown in Fig. 9. Comparison of the two figures shows that the central difference formulation is closer to the reference result at any given resolution, and consequently this method is adopted for the transient calculations. The strengths of the second-order backward method are most pronounced for steady state, Newtonian conditions, where they possess a distinct advantage in providing a very stable solution scheme.

A further example that demonstrates the robustness of the central difference approach is seen in using a rough surface profile in a stationary roughness configuration. The case considered has an elliptical contact corresponding to the crowned axially ground discs used for scuffing experiments at Cardiff [**17**]. Rolling and sliding is in the minor axis direction and the lay of the surface finish orientation is transverse to the entrainment direction in order to replicate the kinematic conditions typically found in gears. The conditions used for the analysis are given in Table 2 and give rise to a smooth surface film thickness of 0.48 μm, and the rough surface utilized for this stationary roughness example has an R_a value of 0.08 μm. Figure 10 shows the results obtained with a mesh having $\Delta x = a/50$ and $\Delta y = a/50$ using the central difference and second-order backward difference methods to approximate the first-order spatial derivatives in the Reynolds equation. The converged film thickness obtained with the second-order backward method can be seen to have physically unacceptable features. The film thickness is predicted to increase systematically in the entraining direction,

Downloaded from pij.sagepub.com at Cardiff University on April 4, 2012

Table 2 Specification of rough-on-smooth eliptic contact conditions

R_x (mm)	19.05
R_y (mm)	150.5
$\bar{U}$ (m/s)	25
E' (GPa)	227.3
w (N)	962
p_{hz} (GPa)	1.05
ξ	0.25
α (GPa^{-1})	11.1
η_0 (Pa s)	0.005
τ_0 (MPa)	10
λ (GPa^{-1})	1.683
γ (GPa^{-1})	2.266
χ (GPa^{-1})	5.1
κ (Pa s)	63.15×10^{-6}

which cannot be physically correct for this stationary roughness case. The transverse pressure gradients are such as to move fluid away from the entrainment axis centre-line illustrated, so that it is clear that in this case the second-order backward method violates the fundamental mass flow continuity that the Reynolds equation is meant to impose on the solution. This is an issue of spatial resolution, as can be seen from Fig. 11, which shows the corresponding results when the mesh spacing is reduced in the x direction to $\Delta x = a/300$, and clearly illustrates that both methods give identical results at this finer resolution.

A formal mathematical error analysis has not been carried out for this highly non-linear problem. The authors have been content to verify the accuracy of the numerical predictions by comparing results obtained with different temporal and spatial resolution to establish the resolution level necessary to produce results that are mesh independent as far as their engineering implications are concerned. This process is illustrated in Fig. 2 for the steady state case and in Figs 7, 8 and 9 for transient analyses of surfaces with a moving analytically defined surface feature. For the case of rough surfaces the issue of time and space resolution is the same for the current analyses as for corresponding line contact analyses reported by the authors in reference [**3**]. The comparisons made in that paper show that the values of Δt and Δx adopted for the current rough surface study are sufficiently fine for the engineering purpose of the analysis. The issue of resolution in the transverse, y, direction for this rough surface modelling is discussed in the companion paper which follows [**18**].

Figure 12 compares the central difference film thicknesses obtained for mesh resolutions of $\Delta x = a/50$ and $\Delta x = a/300$. It shows that the coarse resolution provides a result that is consistent with the fine resolution result taking into account the fact that the surface roughness is essentially resolved differently with a coarser mesh. This steady state comparison is disquieting if second-order backward difference methods are to be utilized for analysing rough surfaces. Their inability to maintain continuity when resolving roughness features relatively coarsely suggests that exceedingly fine meshes need to be used to ensure that continuity is maintained. Since this resolution is related to the roughness features and not to the Hertzian dimension, results obtained in this way for rough surfaces may be questionable. The results of the

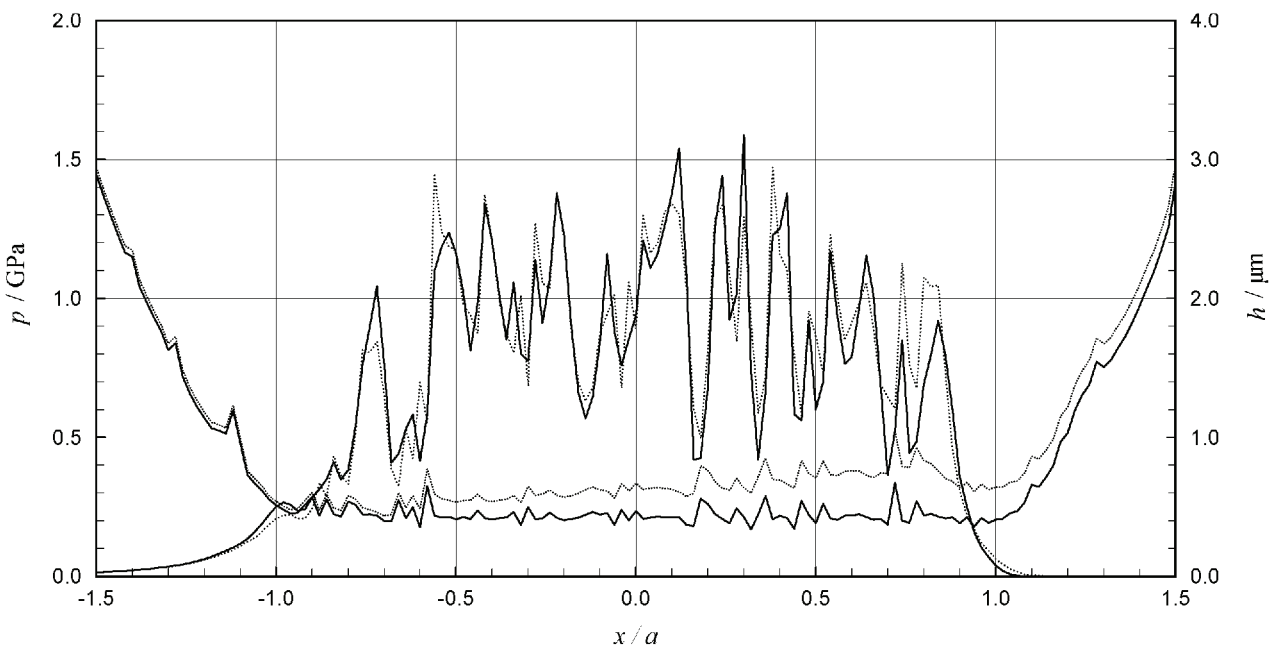

Fig. 10 Comparison of pressure (upper curves) and film thickness (lower curves) results obtained with a stationary rough surface and a moving smooth surface using (———) central differences and (·····) second-order backward differences with $a/\Delta x = a/\Delta y = 50$

Downloaded from pij.sagepub.com at Cardiff University on April 4, 2012

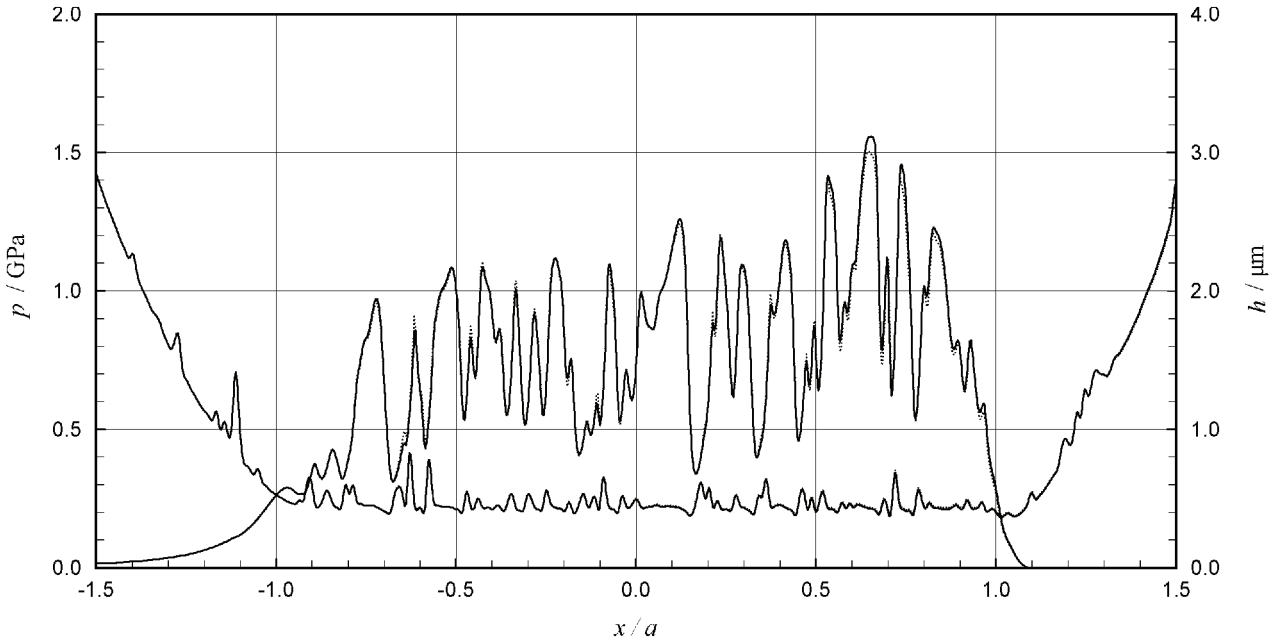

Fig. 11 Comparison of pressure (upper curves) and film thickness (lower curves) results obtained with a stationary rough surface and a moving smooth surface using (———) central differences and (·····) second-order backward differences with $a/\Delta x = 300, a/\Delta y = 50$

comparisons of discretization methods made in this paper, for the differential deflection technique, therefore suggest that the preferred scheme incorporates a Crank–Nicolson approach for the squeeze-film term together with a central difference representation of the spatial derivatives. The latter may be usefully replaced by a second-order backward difference representation of the first-order spatial derivatives for the (special) case of steady state pure rolling conditions at heavy loads.

Discretization of the Reynolds equation by the FE method is found to be almost exactly equivalent to the central difference formulation for all of the test cases considered in the present paper [**15**]. A comparison in the current paper has been made between different finite difference schemes so as not to cloud the issues discussed

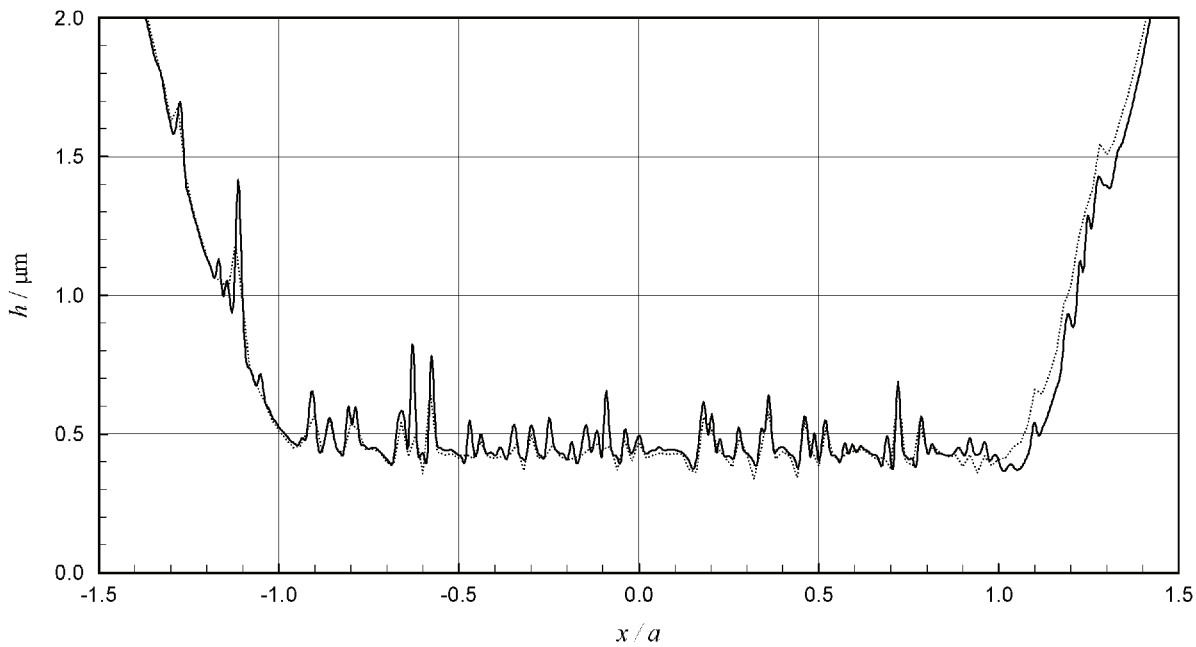

Fig. 12 Comparison of the film thickness results obtained with a stationary rough surface and a moving smooth surface using central differences with (———) $a/\Delta x = 300, a/\Delta y = 50$ and (·····) $a/\Delta x = a/\Delta y = 50$

 © IMechE 2003
Downloaded from pij.sagepub.com at Cardiff University on April 4, 2012

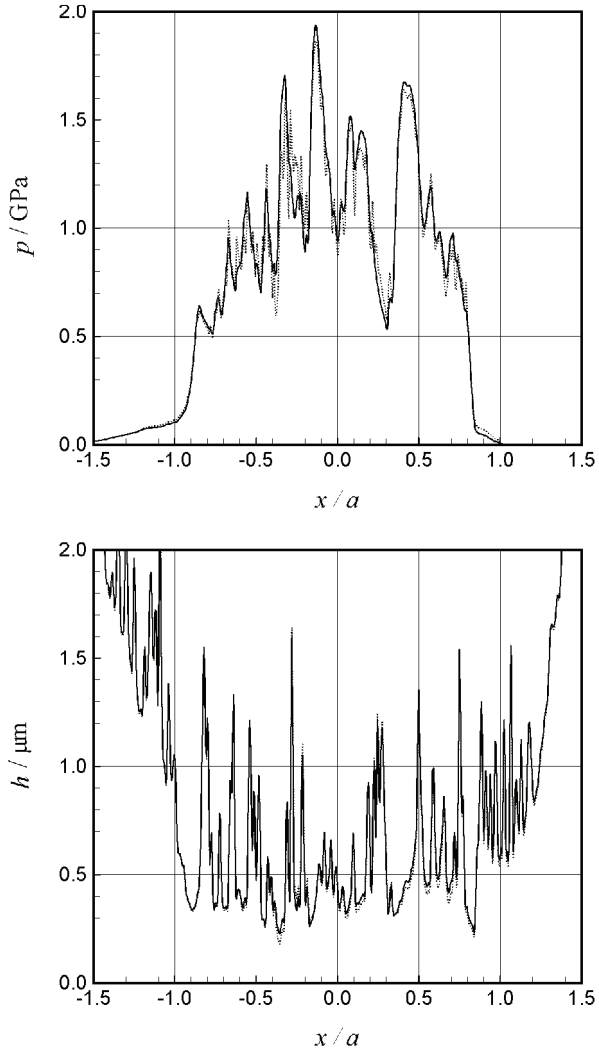

Fig. 13 Comparison of pressure (upper figure) and film thickness (lower figure) at a particular timestep for the transient analysis of two rough surfaces with (———) the FE formulation and (·····) the central difference formulation

in this paper by comparing results obtained using an FE formulation with ones based on finite difference (FD) techniques. Differences between the central FD and FE discretizations begin to appear when a transient analysis of rough surfaces is considered. Figure 13 shows entrainment centre-line comparisons of the pressure and film thickness at one timestep of such an analysis using these two alternative discretization approaches. The case considered is of two rough surfaces in EHL contact. Both bodies have the surface roughness features taken from the roughness profile illustrated in Fig. 14. The profile is taken from a test disc used in scuffing experiments. This disc is finished by transverse grinding and has undergone a degree of asperity modification due to plastic deformation during 'running-in' under load. The profile has a roughness average, $R_a = 0.32\,\mu m$, and the rounded nature of the prominent asperities brought about by the running-in process leads to a skewed

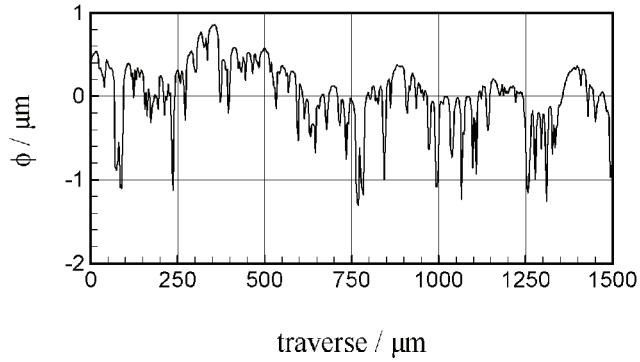

Fig. 14 Roughness profile used for the analyses illustrated in Figs 13 and 15. The profile is illustrated with the metal below the profile trace

distribution of surface heights. In the EHL model this finish is extruded across the whole contact in the transverse, y, direction, so that the surface roughness features are orientated at right angles to the rolling/sliding direction. In this way the analysis models the orientation of roughness features in ground involute gearing applications that are the focus of the research project. The conditions analysed are again as given in Table 2, which leads to a contact semi-dimension in the x direction of 0.34 mm. The mesh size is $\Delta x = a/200$ so that mesh points are 1.7 μm apart. This means that the asperity centred at a traverse position of 690 μm in Fig. 14, which can be regarded as typical, is about 43 μm long from valley to valley and is thus resolved by 25 mesh points.

For the rough surface analysis the timestep adopted is that which causes the faster moving surface to move through one mesh spacing, Δx, in two timesteps. Although the slide–roll ratio considered for the current paper is limited to $\xi = 0.25$, the method behaves in the same way as the corresponding line contact solution. For the line contact case an extensive range of sliding speeds has been used for analysis, with no signs of numerical instability for high sliding speeds [**3**–**5**]. Small differences are seen in the film thickness calculated using the two discretization methods, although there is no significant change. The calculated pressure for the finite difference formulation can be seen to respond more closely to individual roughness features than the corresponding FE analysis. With the FD formulation the finite difference equations are satisfied exactly at the mesh points, without reference to the space between them. The basis of the FE method is that the residual of the equation over the whole of the finite element is minimized in the solution. This difference in emphasis is inherent in the methods and is seen practically in the A_k and B_k coefficients in equation (9). With the FE method these coefficients are all non-zero so that all neighbouring points are involved in the algebraic representation of the Reynolds equation. With the FD version there is no contribution to the equation from the four diagonal neighbours to the mesh point.

Downloaded from pij.sagepub.com at Cardiff University on April 4, 2012

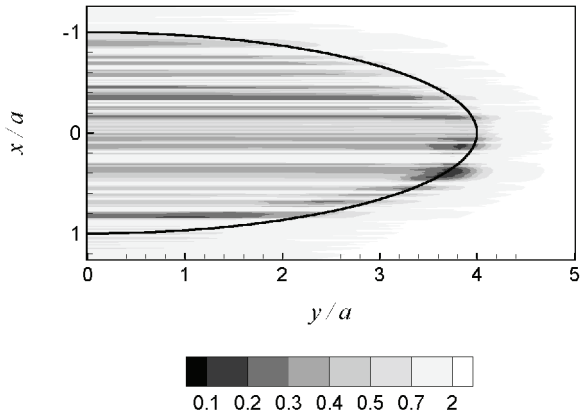

Fig. 15 Film thickness contours (μm) for the case illustrated in Fig. 13 using the FE formulation. The smooth curve indicates a Hertzian dry contact area

The differences between solutions will of course diminish as the resolution is made finer, but finer spatial meshes imply finer timesteps, so that compromise on mesh resolution seems inevitable in the transient study of rough engineering surfaces. The FE formulation is therefore preferred for transient rough surface problems where it is unlikely that meshes that resolve each individual roughness feature very finely will be realistic. Consequently, the FE method with its minimization of the integrated residual can be expected to provide results that are less sensitive to the exact location of the digitization points on the rough surface profile.

Up to this point the results presented in this paper have been in the form of sections on the entrainment centre-lines of the various transient point contact conditions studied to validate the method. Figure 15 shows the contours of film thickness for the transient rough-on-smooth contact considered in Fig. 13. The timestep shown illustrates the severe edge thinning that occurs at the transverse edge of the contact. For this example the smooth surface result has a minimum film thickness of 0.42 μm, which is reduced to 0.1 μm at the transverse edge of the Hertzian contact area for the timestep shown. This is due to the ease with which lubricant can escape from the valley features near the transverse extremes of the contact area, and is the basis of the mechanism for scuffing failure proposed by the authors in a much earlier paper [**19**]. This important side leakage effect is discussed in Part 2 which follows [**18**], where contacts in which both surfaces are rough are considered and asperity collisions that lead to localized and momentary asperity 'dry' contact are observed.

5 CONCLUSIONS

1. The differential deflection technique presented by Evans and Hughes [**1**] has been incorporated into a point contact solution method.
2. A coupled iterative approach has been presented that allows simple (point) iteration to obtain solutions to a complete range of point contact problems.
3. The methods have been validated by detailed comparisons with established results in the tribology literature.

ACKNOWLEDGEMENTS

The support of the EPSRC in providing a studentship under Grant GR/L90996 and a subsequent RA position under Grant GR/N33522 has been instrumental in allowing this study to take place, and is gratefully acknowledged.

REFERENCES

1 **Evans, H. P.** and **Hughes, T. G.** Evaluation of deflection in semi-infinite bodies by a differential method. *Proc. Instn Mech. Engrs, Part C: J. Mechanical Engineering Science*, 2000, **214**(C4), 563–584.

2 **Hughes, T. G., Elcoate, C. D.** and **Evans, H. P.** Coupled solution of the elastohydrodynamic line contact problem using a differential deflection method. *Proc. Instn Mech. Engrs, Part C: J. Mechanical Engineering Science*, 2000, **214**(C4), 585–598.

3 **Elcoate, C. D., Evans, H. P., Hughes, T. G.** and **Snidle, R. W.** Transient elastohydrodynamic analysis using a novel coupled differential deflection method. *Proc. Instn Mech. Engrs, Part J: J. Engineering Tribology*, 2001, **215**(J4), 319–337.

4 **Tao, J., Hughes, T. G., Evans, H. P., Snidle, R. W., Hopkinson, N. A., Starbuck, J.** and **Talks, M.** Elastohydrodynamic lubrication of gear teeth in micropitting tests. *Trans. ASME, J. Tribology*, 2003 (to appear).

5 **Tao, J., Hughes, T. G., Evans, H. P.** and **Snidle, R. W.** Elastohydrodynamic response of transverse ground gear teeth. In Proceedings of the 28th Leeds–Lyon Symposium on *Tribology*, Vienna, 2002, pp. 447–458 (Elsevier, Amsterdam).

6 **Venner, C. H.** and **Lubrecht, A. A.** Numerical simulation of a transverse ridge in a circular EHL contact under rolling/sliding. *Trans. ASME, J. Tribology*, 1994, **116**, 751–761.

7 **Dowson, D.** and **Higginson, G. R.** *Elastohydrodynamic Lubrication*, 1966 (Pergamon Press, Oxford).

8 **Jiang, X., Hua, D. Y., Cheng, H. S., Ai, X.** and **Lee, S. C.** Mixed elastohydrodynamiclubrication model with asperity contact. *Trans. ASME, J. Tribology*, 1999, **121**, 481–491.

9 **Okamura, H.** A contribution to the numerical analysis of isothermal elastohydrodynamiclubrication. In Proceedings of the 9th Leeds–Lyon Symposium on *Tribology*, *Tribology of Reciprocating Engines*, Leeds, 1982, pp. 313–320 (Butterworths, London).

10 **Houpert, L. G.** and **Hamrock, B. J.** Fast approach for calculating film thicknesses and pressures in elastohydrodynamically lubricated contacts at high loads. *Trans. ASME, J. Tribology*, 1986, **108**, 411–420.

11 **Sharif, K. J., Kong, S., Evans, H. P.** and **Snidle, R. W.** Contact and elastohydrodynamic analysis of worm gears. Part 1: theoretical formulation. *Proc. Instn Mech. Engrs,*

Downloaded from pij.sagepub.com at Cardiff University on April 4, 2012

Part C: J. Mechanical Engineering Science, 2001, **215**(C7), 817–830.

12 **Brandt, A.** and **Lubrecht, A. A.** Multilevel matrix multiplication and fast solution of integral equations. *J. Comput. Phys.*, 1990, **90**, 348–370.

13 **Liu, S., Wang, Q.** and **Liu, G.** A versatile method of discrete convolution and FFT (DC-FFT) for contact analyses. *Wear*, 2000, **243**, 101–111.

14 **Johnson, K. L.** and **Tevaarwerk, J. L.** The shear behaviour of elastohydrodynamic oil films. *Proc. R. Soc. Lond.*, 1977, **A356**, 217.

15 **Holmes, M. J. A.** Transient analysis of the point contact elastohydrodynamic lubrication problem using coupled solution methods. PhD thesis, Cardiff University, 2002.

16 **Sharif, K. J., Barregan de Ling, F. de M., Martin, M. J., Alanou, M. P., Evans, H. P.** and **Snidle, R. W.** Film thickness predictions for elastohydrodynamic elliptical contacts over a wide range of radius ratios. *Proc. Instn Mech. Engrs, Part J: J. Engineering Tribology*, 2000, **214**(J1), 63–78.

17 **Patching, M. J., Kweh, C. C., Evans, H. P.** and **Snidle, R. W.** Conditions for scuffing failure of ground and superfinished steel disks at high sliding speeds using a gas turbine engine oil. *Trans. ASME, J. Tribology*, 1995, **117**, 482–489.

18 **Holmes, M. J. A., Evans, H. P., Hughes, T. G.** and **Snidle, R. W.** Transient elastohydrodynamic point contact analysis using a new coupled differential deflection method. Part 2: results. *Proc. Instn Mech. Engrs, Part J: J. Engineering Tribology*, 2003, **217**(J5), 305–321.

19 **Evans, H. P.** and **Snidle, R. W.** A model for elastohydrodynamic film failure in contacts between surfaces having transverse finish. *Trans. ASME, J. Tribology*, 1996, **118**, 847–857.

APPENDIX

The finite difference discretizations utilized are specified in terms of the second- and first-order x-derivative terms in the Reynolds equation:

$$\frac{\partial}{\partial x}\left(\sigma\frac{\partial p}{\partial x}\right) - \bar{U}\left(\rho\frac{\partial h}{\partial x} + h\frac{\partial \rho}{\partial p}\frac{\partial p}{\partial x}\right)$$

The second-order term is represented at point i,j as

$$\frac{\partial}{\partial x}\left(\sigma\frac{\partial p}{\partial x}\right) \approx \frac{(\sigma_{i+1,j}+\sigma_{i,j})(p_{i+1,j}-p_{i,j}) - (\sigma_{i,j}+\sigma_{i-1,j})(p_{i,j}-p_{i-1,j})}{2\Delta x^2}$$

for all formulations. The second term is represented at point i,j in the different formulations as follows:

(a) First-order backward difference

$$\rho\frac{\partial h}{\partial x} + h\frac{\partial \rho}{\partial p}\frac{\partial p}{\partial x} \approx \rho_{i,j}\left(\frac{h_{i,j}-h_{i-1,j}}{\Delta x}\right) + h_{i,j}\left(\frac{\partial \rho}{\partial p}\right)_{i,j}\left(\frac{p_{i,j}-p_{i-1,j}}{\Delta x}\right)$$

(b) Second-order backward difference

$$\rho\frac{\partial h}{\partial x} + h\frac{\partial \rho}{\partial p}\frac{\partial p}{\partial x} \approx \rho_{i,j}\left(\frac{1.5h_{i,j}-2h_{i-1,j}+0.5h_{i-2,j}}{\Delta x}\right) + h_{i,j}\left(\frac{\partial \rho}{\partial p}\right)_{i,j}\left(\frac{1.5p_{i,j}-2p_{i-1,j}+0.5p_{i-2,j}}{\Delta x}\right)$$

(c) Central difference

$$\rho\frac{\partial h}{\partial x} + h\frac{\partial \rho}{\partial p}\frac{\partial p}{\partial x} \approx \rho_{i,j}\left(\frac{h_{i+1,j}-h_{i-1,j}}{2\Delta x}\right) + h_{i,j}\left(\frac{\partial \rho}{\partial p}\right)_{i,j}\left(\frac{p_{i+1,j}-p_{i-1,j}}{2\Delta x}\right)$$

For the time derivative term:

(a) Second-order backward difference

$$\left[\frac{\partial(\rho h)}{\partial t}\right]^m \approx \frac{1.5\rho_{i,j}^m h_{i,j}^m - 2\rho_{i,j}^{m-1}h_{i,j}^{m-1} + 0.5\rho_{i,j}^{m-2}h_{i,j}^{m-2}}{\Delta t}$$

where the superscripts $m-2$, $m-1$ and m indicate consecutive timesteps.

(b) Crank–Nicolson

$$\left[\frac{\partial(\rho h)}{\partial t}\right]^{m-1/2} \approx \frac{\rho_{i,j}^m h_{i,j}^m - \rho_{i,j}^{m-1}h_{i,j}^{m-1}}{\Delta t}$$

In this scheme the spatial terms are the average of their values at the timesteps m and $m-1$.

Downloaded from pij.sagepub.com at Cardiff University on April 4, 2012